

Structures and dynamics of helium in liquid lithium: A study by deep potential molecular dynamics

Xinyu Zhu(朱新宇), Jianchuan Liu(刘建川), Tao Chen(陈涛), Xinyue Xie(谢炘玥), Jin Wang(王进), Yi Xie(谢懿), Chenxu Wang(王晨旭), and Mohan Chen(陈默涵)

Citation: Chin. Phys. B, 2026, 35 (**1**): 013101. DOI: 10.1088/1674-1056/ae15f1
http://cpb.iphy.ac.cn; http://iopscience.iop.org/cpb

What follows is a list of articles you may be interested in

Theoretical study of the light-induced conical intersection in the photodissociation of molecule OH

Jinqian Liu(刘金倩), Jialong Li(李嘉隆), Dongdong Zhang(张栋栋), and Dajun Ding(丁大军)
Chin. Phys. B, 2025, 34 (**10**): 103101. DOI: 10.1088/1674-1056/addcbb

Formation of nanobubbles generated by hydrate decomposition: A molecular dynamics study

Zilin Wang(王梓霖), Liang Yang(杨亮), Changsheng Liu(刘长生), and Shiwei Lin(林仕伟)
Chin. Phys. B, 2023, 32 (**2**): 023101. DOI: 10.1088/1674-1056/ac786a

Effect of conical intersection of benzene on non-adiabatic dynamics

Duo-Duo Li(李多多) and Song Zhang(张嵩)
Chin. Phys. B, 2022, 31 (**8**): 083103. DOI: 10.1088/1674-1056/ac5607

Plasticity and melting characteristics of metal Al with Ti-cluster under shock loading

Dong-Lin Luan(栾栋林), Ya-Bin Wang(王亚斌), Guo-Meng Li(李果蒙), Lei Yuan(袁磊), and Jun Chen(陈军)
Chin. Phys. B, 2021, 30 (**7**): 073103. DOI: 10.1088/1674-1056/abe1a0

Size effect of He clusters on the interactions with self-interstitial tungsten atoms at different temperatures

Jinlong Wang(王金龙), Wenqiang Dang(党文强), Daping Liu(刘大平), Zhichao Guo(郭志超)
Chin. Phys. B, 2020, 29 (**9**): 093101. DOI: 10.1088/1674-1056/ab9619

SPECIAL TOPIC — AI + Physical Science

Structures and dynamics of helium in liquid lithium: A study by deep potential molecular dynamics

Xinyu Zhu(朱新宇)[1,†], Jianchuan Liu(刘建川)[2,†,‡], Tao Chen(陈涛)[1], Xinyue Xie(谢炘玥)[1], Jin Wang(王进)[3], Yi Xie(谢懿)[4], Chenxu Wang(王晨旭)[3], and Mohan Chen(陈默涵)[1,§]

[1] *HEDPS, CAPT, School of Physics and College of Engineering, Peking University, Beijing* 100871, *China*
[2] *School of Electrical Engineering and Electronic Information, Xihua University, Chengdu* 610039, *China*
[3] *State Key Laboratory of Nuclear Physics and Technology, CAPT, Peking University, Beijing* 100871, *China*
[4] *College of Chemistry and Molecular Engineering, Peking University, Beijing* 100871, *China*

(Received 7 August 2025; revised manuscript received 11 October 2025; accepted manuscript online 22 October 2025)

Current experimental techniques still face challenges in clarifying the structural and dynamic properties of helium (He) in liquid lithium (Li). A critical example of this technical hurdle is the formation of He bubbles, which significantly affects the transport of He within liquid Li — a vital aspect when considering liquid Li as a plasma-facing material in nuclear fusion reactors. We develop a machine-learning-based deep potential (DP) with *ab initio* accuracy for the Li–He system and perform molecular dynamics simulations at temperatures ranging from 470 K to 1270 K with a wide range of He concentrations. We observe that He atoms exhibit a tendency to aggregate and form clusters and bubbles in liquid Li. Notably, He clusters exhibit a significant increase in size at elevated temperatures and high concentrations of He, accompanied by the phase separation of Li and He atoms. We also observe an anomalous non-linear relationship between the diffusion coefficient of He and temperature, which is attributed to the larger cluster size at higher temperatures. Our study provides a deeper understanding of the behavior of He in liquid Li and further supports the potential application of liquid Li under extreme conditions.

Keywords: MD simulation, machine-learning-based deep potential, plasma-facing material, He in liquid Li

PACS: 31.15.xv, 31.15.at, 31.15.E, 31.15.es

DOI: 10.1088/1674-1056/ae15f1 **CSTR:** 32038.14.CPB.ae15f1

1. Introduction

Deuterium–tritium (D–T) nuclear fusion is increasingly recognized as a promising future energy source. Since fusion reactors undergo extreme conditions, extensive research on plasma-facing components (PFCs) has been performed.[1–3] Recent studies have identified liquid lithium (Li) as a feasible option for PFCs,[4,5] citing its potential to enhance fusion power output,[6] improve discharge performance,[7] and bolster plasma confinement and overall functionality.[6,8] An in-depth analysis has been conducted on the application of liquid Li in fusion reactors, encompassing both engineering and technological perspectives. This has led to the identification of several challenges that need resolution,[5,9] notably the management of helium (He) retention and recycling within liquid Li environments.[5]

He emerges as the primary by-product in the tritium-breeding process, where neutrons interact with Li atoms, yielding He and tritium.[10–12] Previous simulations have demonstrated that He atoms tend to cluster and form bubbles in liquid Li, thereby impacting tritium mass transfer rates.[13] Furthermore, understanding He behavior in Li is crucial, particularly for the He-cooled Li–Pb fusion blanket,[13,14] because He bubble nucleation can influence the transport of He and hydrogen isotopes,[15] thereby affecting key characteristics in fusion plant applications. Fluid-mechanics-based models have been developed to study the nucleation, growth, and transport of He bubbles in liquid Li.[16,17] However, these studies depend on specific parameters, such as solubility and the diffusion coefficient, derived mainly from experiments[16] and molecular dynamics (MD) simulations.[17] Despite existing experimental efforts to understand He diffusion and trapping in liquid Li,[18,19] additional data are required to resolve remaining uncertainties in nucleation models.[15,16] Some experimental findings are even contradictory, including reports[20] of anomalously low effective diffusion coefficients possibly linked to He bubble nucleation, which require further validation. Moreover, recent studies have indicated that He plasma irradiation significantly alters the corrosion behavior of liquid Li and solid metal surfaces.[20,21] Consequently, investigating the Li–He system through MD simulations is vital to begin unraveling these phenomena and resolving existing contradic-

[†]These authors contributed equally to this work.
[‡]Corresponding author. E-mail: liujianchuan@xhu.edu.cn
[§]Corresponding author. E-mail: mohanchen@pku.edu.cn

© 2026 Chinese Physical Society and IOP Publishing Ltd. All rights, including for text and data mining, AI training, and similar technologies, are reserved.

tions.

Extensive properties of Li have been computed using MD, mainly based on empirical potentials or derived from *ab initio* simulations.[22–28] For instance, various empirical potentials have been developed and employed in MD simulations to study different properties of Li, such as static and dynamic structure factors, yielding good reproduction of certain properties.[22–24] Recently, *ab initio* MD (AIMD) simulations have been utilized to determine the phase diagram of Li under high pressures.[25,26] Additionally, the melting point[27] and dynamic properties[28] of Li can be obtained using AIMD; this approach is independent of empirical parameters but comes at the cost of increased computational resources, especially for larger systems.

The He bubble formation process in liquid Li has been simulated.[29] These studies used the Li–He potential from Soldan[30] and the He–He potential from Aziz.[31] In 2021, nucleation of He in liquid Li under high pressure was observed in MD simulations employing the He–He potential from Aziz.[32,33] MD simulations of a liquid Li–Pb alloy containing He bubbles were performed to extract the diffusion coefficient[34–36] and the pressure–volume relationship[36,37] of He bubbles. In detail, Batet *et al.*[36] analyzed the thermodynamics, structure, and dynamics of Li–He mixtures with different He concentrations at 800 K and pressures ranging from 1 bar to 100 bar using a microscopic model suitable for describing interactions between He and Li at the atomic level. Typically, He–He potentials consider only two-body pair interactions, thereby potentially neglecting some influential many-body effects.[38] However, the majority of these MD simulations rely on classical potentials, whose accuracy and transferability are typically constrained by the analytical forms inherent in such potentials. Consequently, a comprehensive series of systematic tests is needed to ensure reliability; without such validation, these simulations may yield spurious results.[39,40] In this context, developing robust methodologies to optimize potential functions would significantly enhance the accuracy of simulations for the aforementioned systems.[29,37]

With the rapid development of machine-learning (ML) potentials in recent years, several effective methods have been developed to facilitate MD calculations. A typical approach is to derive an atomic interaction potential by fitting a neural network to AIMD data. Such ML-based potentials offer quantum-mechanics-level precision, enabling the quantitative study of various material properties. Additionally, these ML-based potentials are much more efficient than direct AIMD simulations. A variety of ML models have been developed; for example, representative machine-learning interatomic potentials such as the Gaussian approximation potential (GAP)[41] and the deep potential (DP)[42,43] have been systematically and extensively applied in various fields of materials simulation, including irradiation damage, structural phase transitions, and reactions in solution environments, demonstrating excellent applicability and reliability.[44–52] These methods enable large-scale molecular dynamics simulations with near first-principles accuracy, providing valuable tools for understanding complex material behaviors.

In this study, we use the DP method to develop an atomic interaction potential for the Li–He system and to study the static-structure and dynamic properties of Li–He systems with different He concentrations at temperatures ranging from 470 K to 1270 K. We introduce the training and simulation details in Section 2. We discuss the calculated properties in detail in Section 3. Finally, we present the conclusions in Section 4.

2. Methods

2.1. Density functional theory

DFT calculations were performed with the Quantum ESPRESSO package,[53] using the SCAN exchange-correlation density functional[54] and optimized norm-conserving Vanderbilt (ONCV) pseudopotentials.[55] The single-point energies and forces were calculated for the training set with an energy cutoff of 60 Ry. The Γ-point (0, 0, 0) of the Brillouin zone was used to sample the supercell Brillouin zone. All AIMD simulations in this work are based on the above DFT settings.

2.2. Deep potential generation

We use an iterative method to train a DP model. This process is carried out automatically through DP-GEN.[56] Every iteration consists of three stages: exploration, labeling, and training. In the exploration stage, four DP models are used to carry out MD simulations in the chosen systems to explore the potential energy surface (PES) and calculate the energy of every frame. In the labeling process, energy deviation is evaluated, and frames with deviations falling between minimum and maximum thresholds are selected.[57] The energies of these structures are then calculated through DFT. In the training step, the structural information and accurate energy values of the selected frames are incorporated into the training dataset to refine the DP model. Typically, several iterations are required until the deviation becomes sufficiently small. In addition, prior to the first iteration, an initial dataset must be prepared using data obtained from AIMD simulations. The data collection process follows established principles aimed at ensuring a sufficient quantity of data suitable for machine learning in materials science.[58–60] Since the data are sourced directly from DFT and MD calculations, a substantial volume of data can be acquired. To ensure data quality, the principles of completeness and balance[59] are followed through a comprehensive sampling of the PES across varied pressures,

temperatures, and helium concentrations, with a nearly equal amount of data collected for each condition. Next, the principle of consistency[59] is also maintained, as identical parameters are used for DFT calculations both in the initial dataset and during the iterative stage. Additionally, the principle of accuracy[59] is followed, wherein all DFT calculation parameters are tested to ensure convergence. Through this iterative approach, the quantity and quality of the dataset are effectively guaranteed.

In the training part, we describe the concentration of He atoms with β, which is defined as $\beta = n_{\mathrm{Li}}/n_{\mathrm{He}}$, where n_{Li} is the number of Li atoms and n_{He} is the number of He atoms ($\beta = 0$, 0.03, 0.07, 0.10, 0.14, 0.23, 0.33, 0.60, and 1.00). We use an initial dataset containing 50000 frames from AIMD of Quantum ESPRESSO (QE)[61] to train an initial DP model. For the AIMD, we adopt the NVT ensemble ($T = 470$ K, lattice constant = 14.80 Å) to simulate a cubic system containing 128 atoms with $\beta = 0.33$. The time interval is 0.1 fs. The energy cutoff is set to 60 Ry, which has been tested to ensure energy convergence. We adopt the ONCV pseudopotentials[62] and the SCAN exchange–correlation functional.[54]

In the following iterative process, we train the model for 35 iterations. The detailed exploration process is shown in Table 1. We interpret the three stages as follows. In the exploration stage, we use the LAMMPS package[63] to carry out MD calculations with periodic boundary conditions. During the first 10 iterations, temperatures are set to 470 K, 570 K, 670 K, 870 K, 1070 K, and 1270 K, and the temperature increases gradually across successive iterations. In each iteration, the system contains 128 atoms in total, with helium atom concentrations set to $\beta = 0$, 0.03, 0.07, 0.10, 0.14, 0.23, 0.33, 0.60, and 1.00. The NVT ensemble is employed, and an appropriate lattice constant is selected for each structure to maintain the pressure close to 0 GPa. To achieve this, the lattice constant is adjusted for different helium concentrations and temperatures, and the system is relaxed until the average pressure falls below 0.1 GPa. A time step of 0.5 fs is used, and each configuration is sampled over 5000 frames under the respective conditions. For iterations 10–21, the lattice constant is systematically reduced to maintain a pressure near 2 GPa. Similarly, for iterations 22–34, the target pressure is set to approximately 4 GPa. At each temperature, multiple iterations are carried out.

Table 1. Computational details of the 35 iterations (Iter) by using the DP-GEN package. Conditions of the Li–He mixtures during the iterations include the temperature T and the pressure P. The average P values are 0 GP, 2 GP and 4 GPa. For a given P, T increases during the iterations. Nine different concentrations (β, from 0 to 1) of He were explored in every iteration.

Iter (0 GPa)	Iter (2 GPa)	Iter (4 GPa)	T (K)
1, 2, 3	11, 12	23, 24, 25	470
4, 5	13, 14	26, 27	570
6, 7	15, 16	28, 29	670
8	17, 18	30, 31	870
9	19, 20	32, 33	1070
10	21, 22	34, 35	1270

In the labeling stage, we use the Quantum ESPRESSO package to perform all DFT calculations. The energy cutoff is set to 60 Ry, which ensures energy convergence. The energy convergence threshold for the self-consistent calculations is set to 10^{-8}, and only the Γ point is used. We utilize the ONCV pseudopotential.[62] and the SCAN exchange–correlation functional,[54] consistent with the settings in the initial dataset. The minimum threshold for the energy deviation in DP-GEN is set to 10 Ry, and the maximum is 30 Ry. Detailed deviation data are shown in Fig. 1. The ratio of accurate frames remains high throughout most iterations, while the ratio of failed frames is small and close to zero. In this case, approximately 200 additional frames are added to the training dataset during each iteration. Overall, these results indicate that the exploration process is effective.

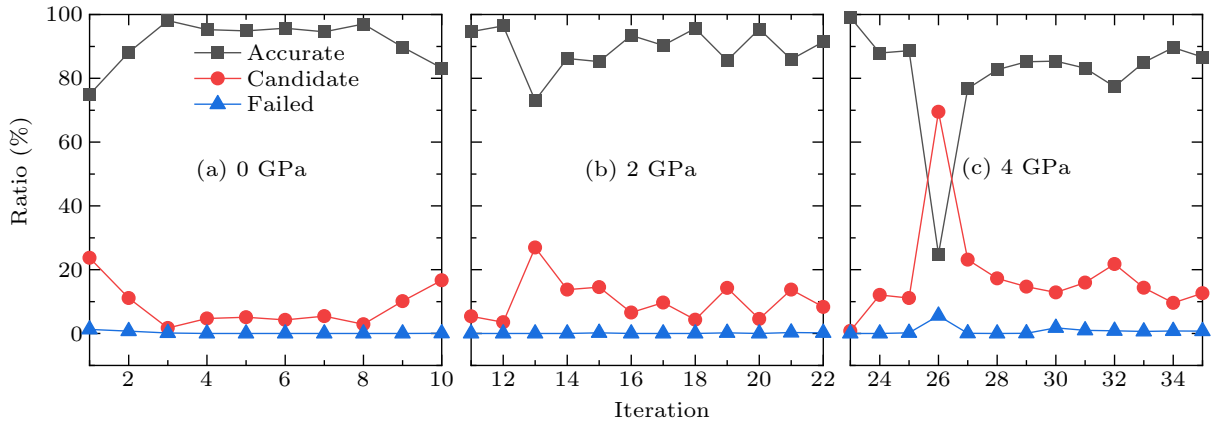


Fig. 1. Ratio of accurate, candidate, and failed frames throughout all iterations. Accurate frames are those with sufficiently high accuracy (deviation lower than 0.10 Ry), whereas failed frames exhibit low accuracy (deviation higher than 0.30 Ry). Candidate frames have intermediate accuracy and are used for training. Panel (a) corresponds to iterations 1–10 at pressures near zero; panel (b) corresponds to iterations 11–22 at pressures around 2 GPa; and panel (c) corresponds to iterations 23–34 at pressures around 4 GPa.

In the training stage, we use the DeePMD-kit package[64] to train the model. We set the cutoff radius to 7 Å and the smooth cutoff to 2 Å. The descriptor network contains 25, 50, and 100 neurons, and the fitting network consists of three layers with 240 neurons each. For every training iteration, the model is optimized for 500000 steps. In our MD simulations, structures with model deviation in the range of $[0.1, 0.3]$ eV/Å are identified as candidate configurations. Up to 200 candidate configurations are selected for each system. These configurations are added to the training set for the next iteration after calculating the energy, forces, and virial tensor using DFT. The dataset is updated iteratively until the proportion of candidate configurations becomes less than 5% and remains nearly unchanged for several consecutive iterations. The validity of these settings is confirmed by MD results obtained from this DP potential, which agree well with previous AIMD simulations and experimental data.

3. Results and discussion

3.1. Benchmarks of the Li–He DP model

First, we validate the accuracy of the DP model. Figures 2(a)–2(f) compare the radial distribution functions (RDFs) of Li–Li obtained from AIMD and DPMD for the pure Li system at different temperatures. We also compare the RDFs of Li–Li, Li–He, and He–He for the Li–He system ($\beta = 0.33$) at 470 K, as shown in Figs. 2(g)–2(i). The RDFs from DPMD simulations agree well with those from AIMD. Furthermore, Fig. 3(a) shows that the diffusion coefficients of liquid Li at zero pressure from DPMD are close to experimental values.[65] Figure 3(b) presents the viscosity of liquid Li from 470 K to 1070 K and compares the results with previous experiments[66,67] and calculations.[28] The DPMD results are consistent with these data across the temperature range. Based on the diffusion coefficients and viscosity, we confirm that DPMD yields accurate dynamic properties consistent with AIMD. Therefore, we consider our DP model sufficiently accurate for evaluating the properties of Li–He systems at 470–1070 K with different He concentrations.

3.2. Density of Li–He mixtures

We perform 5-ps DPMD simulations in the NVT ensemble (constant number of particles N, volume V, and temperature T) for the pure Li system (1024 atoms) at 470 K, 670 K, 870 K, and 1070 K. The cell lengths are adjusted to ensure that the pressure is close to zero for all systems, producing initial simulation configurations.[68] After equilibration, He atoms are randomly inserted into the pure Li system. The He concentration is set to $\beta = 0.031$, 0.062, 0.094, 0.125, and 0.250. To avoid unphysical configurations, the minimum separation between Li and He atoms is constrained to be at least 1.5 Å, based on preliminary simulation results. The cell lengths are further adjusted to maintain zero pressure. Subsequently, 200-ps DPMD simulations are performed in the NVT ensemble for these systems, covering temperatures from 470 K to 1070 K and He concentrations from 0.031 to 0.250.

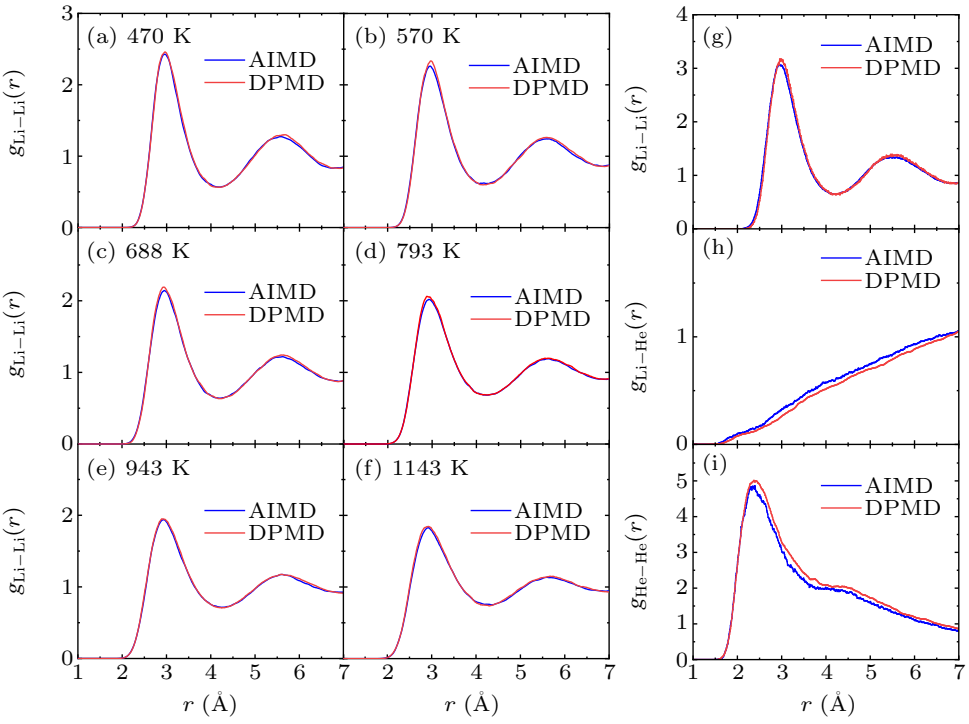


Fig. 2. Properties of liquid Li and Li–He systems obtained from AIMD and DPMD simulations. Panels (a)–(f) show the Li–Li RDFs for pure liquid Li at temperatures ranging from 470 K to 1143 K. Panels (g)–(i) show the RDFs of Li–Li, Li–He, and He–He for the Li–He system at 470 K with $\beta = 0.33$.

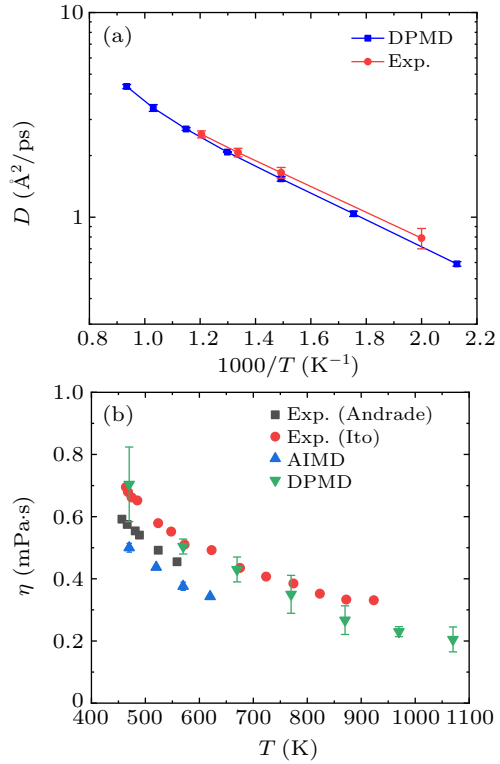


Fig. 3. (a) Diffusion coefficients of liquid Li for the pure Li system at different temperatures. The blue and red lines represent results from DPMD and experiments,[65] respectively. (b) Viscosity of liquid Li at different temperatures. DPMD results are compared with previous AIMD simulations[28] and experimental data.[66,67]

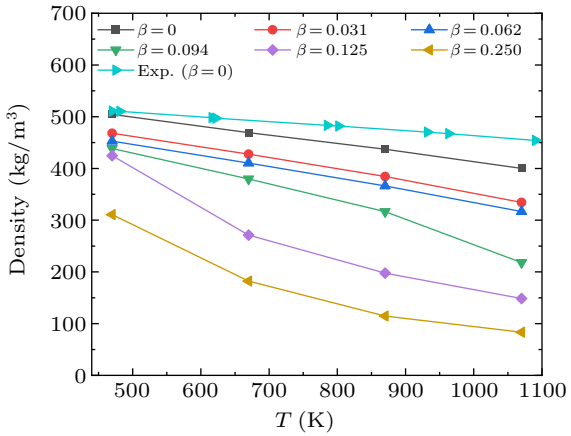


Fig. 4. Ionic density profiles of a Li system under zero pressure across a range of temperatures and He concentrations. The cell contains 1024 Li atoms, and the He concentration varies from $\beta = 0$ to 0.250. Temperatures are set to 470 K, 670 K, 870 K, and 1070 K for different systems. For comparison, experimental data for pure liquid Li are also included.[69]

Figure 4 illustrates the densities obtained from our DPMD simulations together with experimental data[69] across various temperatures and He concentrations. At low He concentrations below $\beta = 0.062$, the density decreases linearly with increasing temperature, which is typical for liquids. For He concentrations above $\beta = 0.125$, the density becomes inversely proportional to temperature, a behavior characteristic of gases that follow Boyle's law. At $\beta = 0.094$ (the green line), the density decrease remains linear up to 870 K, but then drops sharply between 870 K and 1070 K, indicating a transition to a gaseous state caused by He separation and volume expansion, rather than by cluster formation.

However, small discrepancies exist between our DPMD-predicted densities of liquid Li and experimental data.[69] For instance, at 470 K our model underestimates the Li density by 1.2%, and this deviation increases to 11.1% at 1070 K. This discrepancy is mainly attributed to a greater amount of training data around 470 K, which results in better model accuracy within this temperature range. Nevertheless, we consider these differences to be acceptable.

3.3. He clusters under different conditions

Figure 5 shows representative snapshots of liquid Li–He mixtures at various He concentrations ($\beta = 0.031$, 0.062, 0.094, 0.125, and 0.250) and temperatures ($T = 470$ K, 670 K, 870 K, and 1070 K). At $\beta = 0.031$, clusters containing roughly 10 He atoms are observed, and the clustering tendency increases with temperature. Notably, no clusters are found at the highest temperature of 1070 K. A plausible explanation is that the high kinetic energy of He atoms at this temperature prevents them from aggregating into helium bubbles. In contrast, at higher He concentrations, clusters tend to grow in size, while their numbers decrease as temperature increases. For example, at $\beta = 0.062$ and $T = 470$ K, the largest cluster contains fewer than 20 He atoms and coexists with many small clusters. At such low temperatures, the limited mobility of clusters hinders their coalescence. As the temperature increases to 670 K and above, cluster formation becomes more dynamic: multiple clusters containing 10–20 He atoms form, and these clusters merge more easily due to enhanced atomic mobility.

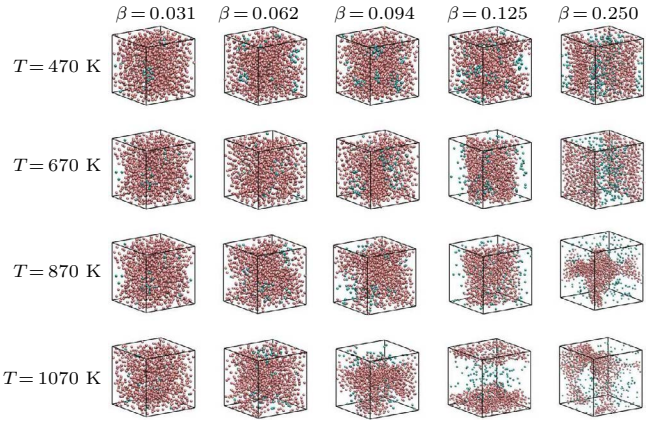


Fig. 5. Snapshots of liquid Li–He mixtures at various He concentrations ($\beta = 0.031$, 0.062, 0.094, 0.125, and 0.250) and temperatures ($T = 470$ K, 670 K, 870 K, and 1070 K). The simulations contain 1024 Li atoms (pink), while He atoms are shown in blue.

As depicted in the snapshots, clusters increase in size with rising temperature. At a He concentration of $\beta = 0.094$, this upward trend in cluster size with temperature is similar to that at $\beta = 0.062$, but the clusters are noticeably larger at the same

temperatures. The number of He atoms in clusters within liquid Li at $\beta = 0.094$ was evaluated at four temperatures: 470 K, 670 K, 870 K, and 1070 K, as shown in Fig. 6. At 470 K, two major clusters containing approximately 25 and 32 He atoms dominate the system. These clusters include nearly all He atoms, with fewer than ten atoms remaining unclustered in the liquid Li. At higher temperatures of 670 K and 870 K, large bubbles with lower atomic density than the surrounding liquid Li emerge, consistent with typical gas-like behavior. At 1070 K, a large bubble containing more than 50 atoms appears, while fewer than 10 atoms are dispersed in the liquid Li. A clear separation between liquid Li and He gas is observed, with He atoms forming an extended, connected region indicative of phase separation.

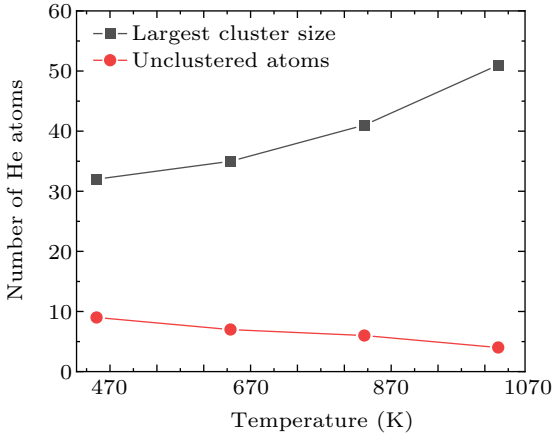


Fig. 6. Number of He atoms in He clusters in liquid Li with a He concentration of $\beta = 0.094$ at 470 K, 670 K, 870 K, and 1070 K.

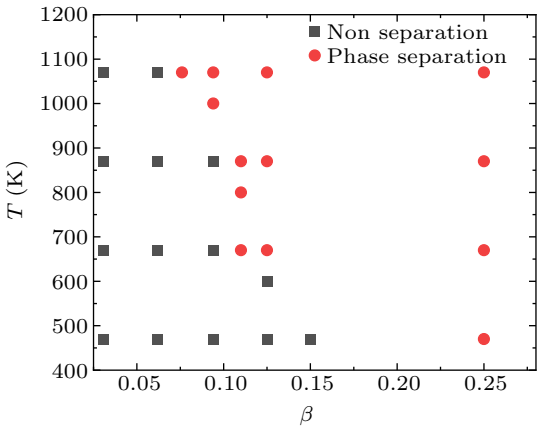


Fig. 7. Diagram depicting the occurrence of phase separation as a function of temperature (T) and He concentration (β). "Phase separation" indicates the transition of He atoms from a dissolved state in liquid Li to a gaseous state, whereas "non-separation" indicates that He remains dissolved in liquid Li.

Heavy segregation of He gas dominates the space, with atoms diffusing rapidly and exhibiting minimal interaction. At He concentrations above $\beta = 0.125$, phase separation is observed at all studied temperatures except for 470 K. At the highest examined concentration, $\beta = 0.250$, phase separation is evident across the entire temperature range. Clusters also tend to grow larger at elevated temperatures and He concentrations, consistent with earlier reports[34] showing that Henry's law constant for He in Li increases with temperature, leading to decreased solubility and larger cluster sizes.[34] In general, phase separation is more likely to occur at high He concentrations and high temperatures, and the onset temperature of phase separation decreases as He concentration increases. Figure 7 illustrates the occurrence of phase separation across various He concentrations ($\beta = 0.031$, 0.062, 0.094, 0.125, and 0.250) and temperatures ($T = 470$ K, 670 K, 870 K, and 1070 K). By performing additional measurements at three intermediate concentrations near the critical region ($\beta = 0.076, 0.110, 0.150$), we can more precisely delineate the phase-separated boundaries. As shown in Fig. 7, when the He concentration β is below approximately 0.076–0.150, phase separation does not occur even at high temperatures. However, when β exceeds this range, phase separation emerges even at relatively low temperatures. Within this critical range ($\beta \approx 0.076$–0.150), the influence of temperature on phase separation becomes significant.

Figure 8 shows the RDFs of Li–Li, Li–He, and He–He at low He concentration ($\beta = 0.031$) and high He concentration ($\beta = 0.250$) at 470 K, 670 K, 870 K, and 1070 K. While the presence of He exerts little influence on the RDFs of Li–Li (Figs. 8(a) and 8(b)) and Li–He (Figs. 8(c) and 8(d)), substantial differences appear in the He–He RDFs (Figs. 8(e) and 8(f)). At $\beta = 0.031$ (Fig. 8(e)), a pronounced peak at about 2.5 Å indicates the clustering tendency of He atoms, with a rapid decay at larger radii. As temperature increases, the peak becomes broader and flatter, suggesting the formation of larger He clusters due to (i) expanded interatomic spacing and (ii) enhanced atomic mobility, which facilitates the growth of larger bubbles. In contrast, at $\beta = 0.250$ (Fig. 8(f)), the flatter RDF profile reflects a more uniform, gas-like distribution of He atoms, corresponding to a clear phase separation into a pure Li liquid phase and a He gas phase.

3.4. Dynamic properties

Self-diffusion coefficients generally follow $D = D_0 \mathrm{e}^{-E/kT}$ for normal gases and liquids in the absence of phase separation.[70] Figure 8 presents the logarithmic diffusion coefficients ($\log(D)$) of Li and He at different He concentrations and inverse temperatures ($1000/T$). For Li (Fig. 9(a)), the linear relation between $\log(D)$ and inverse temperature indicates that the presence of He has only a minor impact on Li mobility. As He concentration increases from $\beta = 0.031$ to 0.250, Li diffusion decreases slightly but remains close to that of pure liquid Li. Conversely, He diffusion (Fig. 9(b)) exhibits a non-linear dependence on temperature, deviating from the expected Arrhenius-like trend due to structural complexity. At $\beta = 0.250$, where phase separation occurs and He behaves as a gas, the relation becomes linear. Sharp increases in the He diffusion coefficient appear at $\beta = 0.125$ between 470 K and

670 K and at $\beta = 0.094$ between 870 and 1070 K, marking the onset of phase separation. After phase separation, He diffusion becomes two orders of magnitude higher, consistent with near-free motion in the gas phase. At lower temperatures and concentrations, where phase separation does not occur, He diffusion remains low. An anomaly is observed at $\beta = 0.062$, where the $\log(D)$ versus $1000/T$ curve is non-linear, indicating a slower-than-expected increase in the diffusion coefficient with temperature and suggesting a potential non-monotonic temperature dependence.

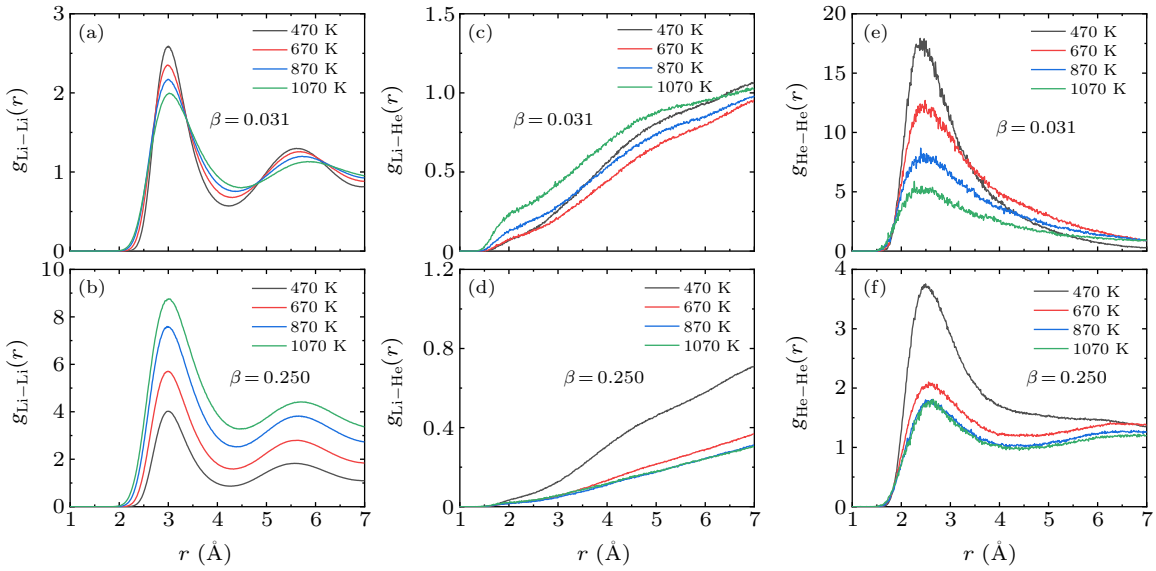


Fig. 8. Partial RDFs for the Li–He system containing 1024 Li atoms at He concentrations of $\beta = 0.031$ and 0.250, representing the minimum and maximum concentrations tested. Panels (a) and (b) show the Li–Li RDFs, panels (c) and (d) show the Li–He RDFs, and panels (e) and (f) show the He–He RDFs, corresponding to $\beta = 0.031$ and 0.250, respectively.

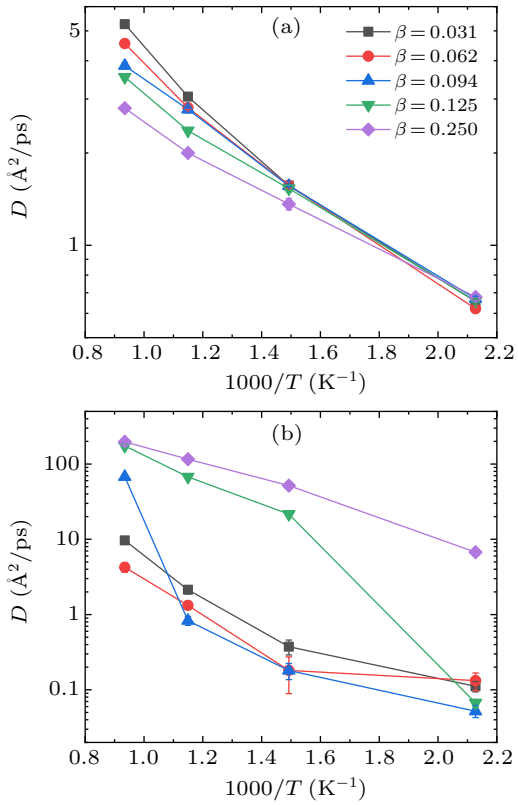


Fig. 9. Diffusion coefficients of (a) Li and (b) He at varying He concentrations and temperatures of 470 K, 670 K, 870 K, and 1070 K for a system containing 1024 Li atoms.

This phenomenon arises from a structural transition in which cluster sizes increase with temperature. For typical liquids or gases, diffusion coefficients ($\log D$) increase linearly with $1/T$. However, at $\beta > 0.062$, the cluster size exhibits a pronounced temperature dependence (see Fig. 4). Larger clusters experience greater resistance to motion within the liquid. As a result, despite the increased kinetic energy provided by heating, the rise in He's diffusion coefficient becomes suppressed. A similar but weaker trend also appears at $\beta = 0.031$, due to the formation of smaller clusters, as discussed in Section 3.3. This explanation extends to $\beta = 0.094$ and $\beta = 0.125$ at 470 K, where substantial cluster formation at even lower temperatures leads to the smallest diffusion coefficients among all systems examined.

Moreover, the diffusion coefficient of He is highly sensitive to cluster size when clusters remain small, but this sensitivity weakens once clusters become sufficiently large. For instance, at $\beta = 0.062$ and $T = 470$ K and 670 K, the cluster size increases from about 5 to approximately 20 atoms, which significantly reduces the slope of the $\log(D)$–$1/T$ relation. Above 670 K, after clusters reach a certain size, the $\log(D)$–$1/T$ relation becomes approximately linear again, as shown in Fig. 8. Further growth of clusters from 20 to over 50 atoms does not markedly alter the diffusion coefficient because the clusters are already too large for additional size effects to be notable. The same behavior appears at $\beta = 0.031$ and $\beta = 0.094$. In particular, at $\beta = 0.094$, clusters remain large across all temperatures, leading to relatively straight lines prior

to phase separation. In summary, cluster growth inhibits mass transport, while increasing temperature enhances atomic mobility and bubble expansion. Once clusters exceed a certain size, the diffusion coefficient increases more slowly, resulting in flatter $\log(D)$–$1/T$ slopes. Additionally, He concentration strongly influences cluster size and diffusion behavior. Following phase separation, diffusion coefficients increase by up to two orders of magnitude, highlighting the complex dynamics of He transport.

4. Conclusion

In this study, we developed a machine-learning-based DP model trained on AIMD data to investigate the static and dynamic properties of He in liquid Li over temperatures ranging from 470 K to 1070 K and He concentrations (β) between 0.031 and 0.250. The model's accuracy is demonstrated by its close agreement with AIMD and experimental data, including density predictions.

Our simulations yield several key findings. First, at low He concentrations and low temperatures, He atoms predominantly form clusters and bubbles within liquid Li. Second, at higher temperatures and He concentrations, both the cluster size and bubble size increase. Furthermore, when the He concentration exceeds $\beta \approx 0.072$–0.166, the system undergoes temperature-independent phase separation into liquid Li and gaseous He. Third, after phase separation, the diffusion coefficient of He rises sharply — by up to two orders of magnitude. Fourth, we identify a nonlinear relationship between the diffusion coefficient and temperature, caused by increasing cluster sizes at elevated temperatures, which moderates the rate of diffusion enhancement. Overall, this study elucidates key features of He behavior in liquid Li and provides insights relevant to the design of liquid PFCs for fusion applications.

Acknowledgments

Project supported by the Excellence Research Group Program for Multiscale Problems in Nonlinear Mechanics of the National Natural Science Foundation of China (Grant No. 12588201), the National Key R&D Program of China (Grant No. 2025YFB3003603), the National Natural Science Foundation of China (Grant No. 12135002), the Fundamental Research Funds for the Central Universities, Peking University, and the Beijing Natural Science Foundation (Grant No. QY23030). The numerical simulations were performed on the high-performance computing platform of CAPT and the "Bohrium" cloud computing platform of DP Technology Co., LTD.

References

[1] Alba R, Iglesias R and Cerdeira M 2022 *Mater.* **15** 6591
[2] Linke J, Du J, Loewenhoff T, Pintsuk G, Spilker B, Steudel I and Wirtz M 2019 *Matter Radiat. Extremes* **4** 056201
[3] Linsmeier C, Unterberg B, Coenen J, Doerner R, Greuner H, Kreter A, Linke J and Maier H 2017 *Nucl. Fusion* **57** 092012
[4] Majeski R 2010 *AIP Conf. Proc.* **1237** 122
[5] De Castro A, Moynihan C, Stemmley S, Szott M and Ruzic D 2021 *Phys. Plasmas* **28** 050901
[6] Eguchi Y, Hyogo H, Ono M, Mizuta T, Ono N, Fujimoto K, Chayama K and Saibara T 2012 *J. Gastroenterol.* **47** 586
[7] Schmitt J, Bell R, Boyle D, Esposti B, Kaita R, Kozub T, LeBlanc B, Lucia M, Maingi R and Majeski R 2015 *Phys. Plasmas* **22** 056112
[8] Maingi R, Boyle D, Canik J, Kaye S, Skinner C, Allain J, Bell M, Bell R, Gerhardt S and Gray T K 2012 *Nucl. Fusion* **52** 083001
[9] Ruzic D, Szott M, Sandoval C, Christenson M, Fiflis P, Hammouti S, Kalathiparambil K, Shchelkanov I, Andruczyk D and Stubbers R 2017 *Nucl. Mater. Energy* **12** 1324
[10] Kordač M and Košek L 2017 *Fusion Eng. Des.* **124** 700
[11] Rubel M 2019 *J. Fusion Energy* **38** 315
[12] Suud Z and Yazid I P 2020 *J. Phys.: Conf. Ser.* **1493** 012003
[13] Fradera J, Batet L, de les Valls E M and Sedano L 2009 *23rd IEEE/NPSS Symp. Fusion Eng.* 1
[14] Gilbert M, Dudarev S, Zheng S, Packer L and Sublet J C 2012 *Nucl. Fusion* **52** 083019
[15] Hassanein A 2002 *J. Nucl. Mater.* **302** 41
[16] Batet L, Fradera J, de les Valls E M and Sedano L 2011 *Fusion Eng. Des.* **86** 421
[17] De Les Valls E M, Sedano L, Batet L, Ricapito I, Aiello A, Gastaldi O and Gabriel F 2008 *J. Nucl. Mater.* **376** 353
[18] Nieto M, Ruzic D, Allain J, Coventry M and Vargas-Lopez E 2003 *J. Nucl. Mater.* **313** 646
[19] Allain J, Nieto M, Coventry M, Stubbers R and Ruzic D 2004 *Fusion Eng. Des.* **72** 93
[20] He P, Zhang Z, Xia W, Shu L, Ma X, Gou F and Zhang K 2018 *J. Nucl. Mater.* **509** 736
[21] He P, Wang Z, Ye Z, Yang L, Gou F and Zhang K 2020 *J. Nucl. Mater.* **539** 152269
[22] González L, González D, Silbert M and Alonso J 1993 *J. Phys.: Condens. Matter* **5** 4283
[23] Canales M, González L E and Padró J A 1994 *Phys. Rev. E* **50** 3656
[24] Torcini A, Balucani U, De Jong P and Verkerk P 1995 *Phys. Rev. E* **51** 3126
[25] Hernández E R, Rodriguez-Prieto A, Bergara A and Alfe D 2010 *Phys. Rev. Lett.* **104** 185701
[26] Yang J, John S T and Iitaka T 2010 *J. Phys.: Condens. Matter* **22** 095503
[27] Chen M, Hung L, Huang C, Xia J and Carter E A 2013 *Mol. Phys.* **111** 3448
[28] Chen M, Vella J R, Panagiotopoulos A Z, Debenedetti P G, Stillinger F H and Carter E A 2015 *AIChE J.* **61** 2841
[29] Insepov Z and Hassanein A 2005 *J. Nucl. Mater.* **337** 912
[30] Soldán P, Lee E P, Lozeille J, Murrell J N and Wright T G 2001 *Chem. Phys. Lett.* **343** 429
[31] Aziz R A and Slaman M J 1991 *J. Chem. Phys.* **94** 8047
[32] Aziz R A, McCourt F R and Wong C C 1987 *Mol. Phys.* **61** 1487
[33] Ávarez-Galera E, Martí J, Mazzanti F and Batet L 2023 *J. Chem. Phys.* **159**
[34] Sedano L 2007 *Materials for Fusion Technology Program*
[35] Hassanein A, Allain J, Insepov Z and Konkashbaev I 2005 *Fusion Sci. Technol.* **47** 686
[36] Alvarez-Galera E, Marti J, Mazzanti F and Batet L 2023 *J. Chem. Phys.* **159**
[37] Fraile A and Polcar T 2020 *Nucl. Fusion* **60** 046018
[38] Parish C A and Dykstra C E 1994 *J. Chem. Phys.* **101** 7618
[39] Seletskaia T, Osetsky Y, Stoller R E and Stocks G M 2008 *Phys. Rev. B* **78** 134103
[40] Zu X T, Yang L, Gao F, Peng S, Heinisch H L, Long X and Kurtz R J 2009 *Phys. Rev. B* **80** 054104
[41] Bartók A P, Payne M C, Kondor R and Csányi G 2010 *Phys. Rev. Lett.* **104** 136403
[42] Zhang L, Han J, Wang H, Car R and Weinan E 2018 *Phys. Rev. Lett.* **120** 143001
[43] Wang H, Guo X, Zhang L, Wang H and Xue J 2019 *Appl. Phys. Lett.* **114** 244101

[44] Klawohn S, Darby J P, Kermode J R, Csányi G, Caro M A and Bartók A P 2023 *J. Chem. Phys.* **159**

[45] Byggmästar J, Hamedani A, Nordlund K and Djurabekova F 2019 *Phys. Rev. B* **100** 144105

[46] Hamedani A, Byggmästar J, Djurabekova F, Alahyarizadeh G, Ghaderi R, Minuchehr A and Nordlund K 2020 *Mater. Res. Lett.* **8** 364

[47] Lu D, Wang H, Chen M, Lin L, Car R, Weinan E, Jia W and Zhang L 2021 *Comput. Phys. Commun.* **259** 107624

[48] Zhang L, Wang H, Car R and Weinan E 2021 *Phys. Rev. Lett.* **126** 236001

[49] Zhang D, Liu X, Zhang X, Zhang C, Cai C, Bi H, Du Y, Qin X, Peng A, Huang J, Li B, Shan Y, Zeng J, Zhang Y, Liu S, Li Y, Chang J, Wang X, Zhou S, Liu J, Luo X, Wang Z, Jiang W, Wu J, Yang Y, Yang J, Yang M, Gong F Q, Zhang L, Shi M, Dai F Z, York D M, Liu S, Zhu T, Zhong Z, Lv J, Cheng J, Jia W, Chen M, Ke G, E W, Zhang L and Wang H 2024 *NPJ Comput. Mater.* **10**

[50] Liu J, Zhang X, Chen T, Zhang Y, Zhang D, Zhang L and Chen M 2024 *J. Chem. Theory Comput.* **20** 5717

[51] Liu J, Chen T, Mao S and Chen M 2025 *Comput. Mater. Sci.* **253** 113825

[52] Chen J, Li J, Xiao X, Qiao H, Yang J, Peng P, Xiao J, Tao M and Liu J 2025 *Surf. Interfaces* **62**

[53] Giannozzi P, Baroni S, Bonini N, Calandra M, Car R, Cavazzoni C, Ceresoli D, Chiarotti G L, Cococcioni M and Dabo I 2009 *J. Phys.: Condens. Matter* **21** 395502

[54] Sun J, Ruzsinszky A and Perdew J P 2015 *Phys. Rev. Lett.* **115** 036402

[55] Hamann D 2013 *Phys. Rev. B* **88** 085117

[56] Zhang L, Lin D Y, Wang H, Car R and E W 2019 *Phys. Rev. Mater.* **3** 023804

[57] Liu Y, Yang Z, Zou X, Lin Y, Ma S, Zuo W, Zou Z, Wang H, Avdeev M and Shi S 2025 *Mater. Sci. Eng.* **166** 101050

[58] Liu Y, Yang Z, Zou X, Ma S, Liu D, Avdeev M and Shi S 2023 *Natl. Sci. Rev.* **10** nwad125

[59] Liu Y, Ma S, Yang Z, Wu D, Zhao Y, Avdeev M and Shi S 2025 *J. Materiomics* **11** 101066

[60] Liu Y, Ma S, Yang Z, Zou X and Shi S 2023 *J. Chin. Ceram. Soc.* **51** 427

[61] Giannozzi P, Baroni S, Bonini N, Calandra M, Car R, Cavazzoni C, Ceresoli D, Chiarotti G L, Cococcioni M and Dabo I 2009 *J. Phys.: Condens. Matter* **21** 395502

[62] Hamann D 2013 *Phys. Rev. B* **88** 085117

[63] Plimpton S 1995 *J. Comput. Phys.* **117** 1

[64] Zhang L, Han J, Wang H, Car R and E W 2018 *Phys. Rev. Lett.* **120** 143001

[65] Blagoveshchenskii N, Novikov A and Savostin V 2012 *Physica B* **407** 4567

[66] Cottrell A H 1972 *Biogr. Mem. Fellows R. Soc.* **18** 1

[67] Ito Y, Minami K and Nagashima A 1989 *Int. J. Thermophys.* **10** 173

[68] Chislett-McDonald S, Surrey E, Naish J, Turner A and Hampshire D 2022 arXiv:2205.04441 [physics.plasm-ph]

[69] Yakimovich K A E and Mozgovoi A G 2000 *High Temp.* **38** 657

[70] Konings R and Stoller R 2020 *Comprehensive Nucl. Mater.* (Elsevier)